جامعة الملك عبدالله
للعلوم والتقنية
King Abdullah University of
Science and Technology

Current status of the high-temperature kinetic models of silane: Part I. Pyrolysis

Item Type	Article
Authors	Chatelain, Karl P.;He, Yizhuo;Alharbi, Reham;Mével, Rémy;Petersen, Eric L.;Lacoste, Deanna
Citation	Chatelain, K. P., He, Y., Alharbi, R., Mével, R., Petersen, E. L., & Lacoste, D. A. (2020). Current status of the high-temperature kinetic models of silane: Part I. Pyrolysis. Combustion and Flame. doi:10.1016/j.combustflame.2020.11.030
Eprint version	Post-print
DOI	10.1016/j.combustflame.2020.11.030
Publisher	Elsevier BV
Journal	Combustion and Flame
Rights	NOTICE: this is the author's version of a work that was accepted for publication in Combustion and Flame. Changes resulting from the publishing process, such as peer review, editing, corrections, structural formatting, and other quality control mechanisms may not be reflected in this document. Changes may have been made to this work since it was submitted for publication. A definitive version was subsequently published in Combustion and Flame, [, , (2020-12)] DOI: 10.1016/j.combustflame.2020.11.030 . © 2020. This manuscript version is made available under the CC-BY-NC-ND 4.0 license http://creativecommons.org/licenses/by-nc-nd/4.0/
Download date	2023-12-06 18:38:01
Link to Item	http://hdl.handle.net/10754/666266

Current Status of the High-Temperature Kinetic Models of Silane: Part I. Pyrolysis

Karl P. Chatelain[a], Yizhuo He[b], Reham Alharbi[a], Rémy Mével[b,c], Eric L. Petersen[d], Deanna A. Lacoste[a]

[a]*King Abdullah University of Science and Technology (KAUST), Clean Combustion Research Center (CCRC), Thuwal, Saudi Arabia*
[b]*Center for Combustion Energy, Tsinghua University, Beijing, China*
[c]*School of Vehicle and Mobility, Tsinghua University, Beijing, China*
[d]*Department of Mechanical Engineering, Texas A&M University, College Station, TX, USA*

Abstract

The present work compares the performance of seven reaction models with respect to a large experimental dataset relevant to the high-temperature pyrolysis of both silane (SiH_4) and disilane (Si_2H_6). Their performances were established based on different validation criteria that account for the shape and the amplitude of the validation profile. Then, the model performances were quantified with a global error, which accounts for the experimental uncertainties. The most satisfactory model has a global error as low as 3.1 (i.e., meaning 3.1 times higher than the experimental uncertainty) and the highest fraction (74%) of criteria with a low error (< 2), while most of the models have large discrepancies with the validation dataset, global error near 8 and up to 110 for the less accurate model. The origins of these discrepancies are identified with reaction pathway and sensitivity analyses. Among the seven tested model, three main decomposition pathways are evidenced, including one more specific to the models presenting the lowest errors. Based on the global error values, the ability to reproduce all the experimental conditions, and the model analyses, the reaction pathways relevant to the high-temperature pyrolysis of silane and disilane are determined. In addition, the present study provides experimental and numerical guidance for the future developments of silicon hydride reaction models. The limited performance of most of the oldest reaction models may have a significant impact on our current understanding of the pyrolysis and oxidation kinetics of silane.

Key words: Chemical Kinetics, Silane, Disilane, Reaction Model

Email address: remy.mevel@tsinghua.edu.cn (Rémy Mével)

1. Introduction

Silane and other small silicon hydrides (Si_xH_y) are involved in the production of a large number of products related to the semi-conductor industry. They are used to manufacture insulation materials [1], silicon nanowires [2], solar panel elements [3], catalysts, and electronic devices. Unlike the hydrocarbon kinetics [4, 5, 6, 7, 8, 9, 10, 11, 12], the kinetics of silicon containing molecules have been less investigated. The need for accurate high-temperature reaction model for silicon hydrides, such as silane and disilane, recently regained interest with the development of high-temperature synthesis techniques for advanced nanomaterials, such as self-propagating high-temperature synthesis (SHS), flame spray pyrolysis (FSP), or combustion synthesis [13]. In addition to its application to materials science, the high-temperature pyrolysis of silicon hydrides is also of interest for risk assessment studies [14, 15] and propulsion [16, 17].

The first silane reaction models were developed for the high-temperature combustion by analogy with the methane combustion, from the pioneering work of Jachimowski and McLain [18], Hartman et al. [19], and Britten et al. [20]. Later, pyrolysis-specific reaction submodels started to be investigated in the 90's. A reaction model composed of 20 reactions was developed for silane and disilane (Si_2H_6) pyrolysis by Mick [21] and Woiki et al.,[22]. This model was later updated by Petersen and Crofton [23]. In addition, several reaction models for silane oxidation kinetics, including pyrolysis submodels, were developped by Babushok et al. [24], Kondo et al. [25], Miller et al. [26], and Mével et al. [27, 28, 29]. Some of these oxidation models also include particles formation pathways, which are of interest for material synthesis processes, such as the chemical vapor deposition (CVD) processes [30]. Recently, new reaction models were developed, such as the updated reaction model of Petersen (also called PeOx, recently presented in [31, 32]), the RMG-based reaction model from Slakman et al. [33], and an updated version of Mével's reaction model, referred to as Chatelain's reaction model in the present work [34]. While all these oxidation reaction models include silane pyrolysis submodels, their validity have never been thoroughly demonstrated under pyrolysis conditions. Due to possible extreme conditions (high-temperature and equivalence ratio variations) encountered in the aforementioned new synthesis methods, i.e. SHS, FSP, and combustion synthesis, the evaluation of reference reaction models for silane kinetics is needed. In fact, the kinetics of solid material precursors must be understood and validated before modeling the solid particle formation. This approach is in line with the work done in autoxidation [35, 36, 37] or the soot formation in flames [38, 39, 40], where

the kinetics of precursors has a key role in the solid particle formation. In addition, this evaluation of small silicon hydride kinetics may benefit the development of reaction models for the high-temperature kinetics of larger silicon hydrides [41, 42, 43].

This comprehensive study aims to evidence the current status of silane chemical models on both pyrolytic and oxidative conditions. For clarity sake, this work is divided into two standalone studies. The first study aims to perform an exhaustive evaluation of seven reaction models against an extensive validation dataset composed of 85 experimental conditions representative of the high-temperature pyrolysis of silane and disilane. The performance of the reaction models was quantitatively determined based on the methodology proposed by Olm et al. [44]. As this methodology considers the experimental uncertainties, this approach is more reliable to quantify the performance of reaction models compared to the typical error calculation methods (such as the relative error or the sum of the square root calculation methods), commonly applied in conventional model validations studies [8, 9, 11, 31, 32]. The second study [45] employs the same reaction models and the same assessment methodology on an extensive validation dataset (composed of 230 conditions) relevant to the high-temperature oxidation of silane by various oxidizers.

2. Methodology

2.1. Validation data-set

The validation dataset compiles experimental data relevant to both silane and disilane pyrolysis. As summarized in Table 1, the collected data are composed of time- and temperature-resolved profiles for the following species: SiH_4, SiH_2, SiH, Si, and H, obtained in the following experimental conditions: X_{SiH_4} or $X_{Si_2H_6} = 0.2 - 1000$ ppm, $X_{H_2} = 0 - 15$ %, $X_{Ar} \approx 85$ % – >99.99 %, $T = 1110 - 2934$ K, and $P = 30 - 500$ kPa where X, T, and P refer to the mole fraction, the temperature, and the pressure, respectively. These data mainly cover the high-temperature conditions for highly-diluted silane and disilane mixtures, obtained from different research groups [21, 23, 46, 47, 48, 49, 50, 51, 52] with different shock-tube facilities and diagnostic techniques. The validation dataset mainly comprises highly-diluted conditions, which are known to minimize the role of secondary reactions in the reactive system. Detection techniques like atomic resonance absorption spectroscopy (ARAS), frequency modulation spectroscopy (FMS), and direct emission and absorption methods were used to measure the different temporal evolution of species during the experiments, while specific species ratios were used for the temperature-resolved profiles (e.g. X_I/X_R where I and R are an intermediate species and

the reactant, respectively). Mick et al.[21] and Markus and Roth [48] measured the temporal evolution of Si atoms and of SiH_2 during Si_2H_6 pyrolysis using ARAS and laser absorption, respectively. Crofton and Petersen [52] reported temporal evolution of SiH_2 profiles during Si_2H_6 pyrolysis obtained with the FMS technique. Petersen et al. [23, 50, 51] proposed an updated rate constant for the thermal decomposition of SiH_4, based on silane IR emission profiles. Crofton and Petersen [23, 52] reported SiH_2 profiles obtained during SiH_4 pyrolysis, using both the laser absorption and FMS techniques. Mick [21] and Markus and Roth [49] used laser absorption methods to measure SiH profiles during SiH_4 pyrolysis. Mick et al. [21, 46, 47] reported Si and H atom concentrations during silane pyrolysis.

The 85 experimental conditions compiled in this dataset are represented in 37 individual validation figures in total, which comprise 27 time- and 10 temperature-resolved figures.

Table 1: Experimental conditions used for the reaction model validation. The mole fraction balance is the argon fraction.

	# exp. data	X_{SiH_4} **[ppm]**	X_{H_2} **[%]**	$X_{Si_2H_6}$ **[ppm]**	T **[K]**	P **[kPa]**	**Species profiles**	**Reference**
SiH_4	54	0.2 - 1000	0 - 0.1	0	1205 - 2934	65 - 500	Si, SiH_4, H, SiH_2, SiH	[21, 23, 46, 47, 49, 50, 52]
Si_2H_6	31	0 - 500	0 - 15	0.2 - 100	1072 - 2185	30 - 130	Si, SiH_2	[21, 48, 52, 53]

2.2. Kinetic models and numerical tools

The different reaction models compared in the present study are presented in Table 2, with their total size (Total), their relative size for pyrolytic conditions (Pyro.), and the size of their common submodels ($OH^\star$ and nitrogen species ($N_xH_yO_z$) chemistry).

Table 2: List of the reaction models evaluated in the present study. For each reaction model, both their total (Total) and relative size relevant to the pyrolytic conditions (Pyro.) are indicated. The size for pyrolytic conditions is determined by removing all oxygen, nitrogen, and carbon containing molecules and reactions, except N_2.

Reaction model	**Species**		**Reactions**		**Common submodels** ($OH^\star$ and nitrogen chemistry)
	Total	Pyro.	Total	Pyro.	
Chatelain	86	18	425	19	
Mével	92	19	448	19	
PeOx	166	21	1159	55	31 species, 177 reactions
Babushok	65	21	380	55	
Kondo	94	17	322	7	
Miller	91	17	371	30	
Slakman	-	83	-	2708	-

Chatelain's reaction model (Chatelain) is an improved version of Mével's reaction model (Mével)

in terms of chemical kinetics consistency [34]. Applying the methodology presented in [34], the thermodynamic data of 30 species, 13 reactions, 2 species mislabeling, and 2 thermodynamic discontinuities were corrected from the original mechanism (i.e., Mével's reaction model). A limited qualitative comparison between Chatelain's and Mével's reaction model was performed in [34] and tend to indicate better performance of Chatelain's model. As the present study employs a more comprehensive comparison of the models, with quantitative analyses, it aims to corroborate or refute our preliminary conclusion. Crucially, some of the inconsistencies (species mislabeling and thermodynamic discontinuity) identified in Mével are also present in reference reaction models, as presented in [34].

Petersen's reaction model (PeOx) is an updated version of the former reaction model developed by Petersen's group along their series of work on silane kinetics [23, 50, 51, 54, 55], initially based on the work of Babushok [24]. This recent reaction model was briefly presented and tested for the first time by Chatelain et al. [31, 32]. As seen in Table 2, this reaction model is large compared to most of the other reaction models. Contrary to all the other reaction models, PeOx is not limited to Si-containing molecules kinetics. In fact, it includes not only silane and disilane kinetics but also includes multiple submodels for hydrocarbons (alkanes, aromatics, naphtenes, and olefins) up to C_6.

Slakman's reaction model [33] (Slakman) is the first reaction model for silicon-containing molecules developed with RMG [56], which is an automated reaction mechanism generator. This reaction model was developed exclusively for pyrolytic conditions and includes both silane and disilane chemistry. The silicon-specific database was generated based on thermochemical data and reaction rates available in the literature, as well as some newly calculated hydrogen abstraction reaction rates. Due to the automated model generation, this reaction model is the largest mechanism among the seven evaluated, due to the large number of isomers (regio-isomers and electronic state distinctions) included into it. This mechanism includes many pressure dependent reactions, using Chebyshev formalism, for which the polynomial coefficients are defined on a specific temperature range (below 2000 K in this model). More detailed information on Chebyshev formalism are available in Chemkin [57], Cantera [58], or RMG [59] documentations. Thus, Slakman's reaction model cannot reproduce the experimental conditions above 2000 K (38 out of the 85 experimental conditions). Although a reaction model without pressure dependent reactions is also available in their study, it is significantly less performant than the one with pressure dependent reactions as shown in their study [33]. For this reason, the mechanism with pressure dependent reactions, named "PDep_y0" in their supplementary materials, was chosen.

Mével's [28, 29], Babushok's [24], Kondo's [25], and Miller's [26] models are four reference reaction

models for silane kinetics. Mével's reaction model contains submodels to be representative of SiH_4 and Si_2H_6 pyrolysis, as well as the oxidation kinetics of SiH_4 by oxygen, nitric oxide, and nitrous oxide. Mével's model was developed based on the work of Babushok [24], Miller [26], and the early work of Petersen [23, 50, 51, 54, 55]. Babushok's and Kondo's reaction models were developed and validated against ignition delay, flame speed, and explosion limit data of silane, mostly for safety-relevant conditions (room temperature and atmospheric conditions). Due to their interest in the low temperature conditions, the development of these mechanisms were based on the previous work of Jachimovski and McLain [60] and Britten et al. [20] with a focus on identifying low activation energy pathways through the SiH_3 radical peroxidation ($SiH_3 + O_2 \longrightarrow SiH_3OO$) and cyclic intermediates. Crucially, these two reaction models are not available in the literature anymore, as the link referring to Babushok's model in [24] is not active anymore and Kondo's model was not provided in their supplementary materials. While Babushok's reaction model was obtained before the link deactivation, Kondo's reaction model was reconstructed based on the reactions listed in Kondo's work [25] and the thermochemical data from Miller [26]. Miller's reaction model is an extended and updated version of pre-existing reaction models [61, 62], based on ab-initio calculations. This model was specifically validated to reproduce both low- and high-temperature silane chemistry for a wide range of temperature and pressure. It is recognized that the model of Kondo was initially developed to reproduce the low-temperature spontaneous ignition of silane in air. Thus, it is not necessarily expected that it can predict high-temperature pyrolysis very accurately. Nevertheless, it is interesting to quantify its performance. Examples presenting the objective function calculations for the different criteria are provided in supplementary materials.

In order to keep the reaction models unchanged for the silane oxidation study, all the reaction models have common $OH^\star$ and nitrogen chemistry submodels, respectively from Hall et al. [55] and Mével et al. [29]. The $OH^\star$ submodel from Hall et al. [55] was updated with the reaction from Hidaka et al., $N_2O + H = OH^\star + N_2$ [63], which was present initially in the $OH^\star$ submodel from Mével et al. [29]. These two submodels were not added to Slakman's reaction model, as this reaction model is only developed for the silane pyrolysis and has no oxidation submodel.

All the simulations and analyses (Rate of Production (RoP) and sensitivity analyses) were conducted using ANSYS [57] software (Chemkin-Pro). Simulations were performed with a closed homogeneous reactor (*CKReactorGenericClosed*) and an adiabatic constant volume reactor (*CONV*).

As some of the present models are not anymore easily accessible in the literature, the different

mechanisms used in the present validation are provided in supplementary materials.

2.3. Assessment of the performance

2.3.1. Presentation of the validation criteria

To easily compare the performances of each mechanism, five different validation criteria were extracted from each experimental and simulated data, based on the type of data available, as summarized in Table 3 and presented in Fig. 1. The criteria are defined as follow: C1, C2, and C3 are the delay to the peak maximum, the delay to 50% of the peak maximum (before the maximum), and the delay to 50% of the peak maximum (after the maximum) for a given time-resolved validation figure, respectively (see Fig. 1a); C4 corresponds to the area integration (area under the curve) of the signal over the experimental observation time or temperature range for a given time- (see Fig. 1a) and temperature-resolved (see Fig. 1b) validation figure, respectively; C5 corresponds to the temperature dependence (the slope) of the validation parameter employed in a given temperature-resolved validation figure (see Fig. 1b). These criteria characterize the overall signal: criteria C1, C2, C3, and C5 account for the overall shape (by defining the peak positions or the slope); C4 represents the quantity produced of the validation parameter. Note that only a single pair of C4 and C5 criteria are calculated per temperature-resolved validation figure, while it involves multiple experimental conditions. As seen in Table 3, each criterion is not extracted from each validation figure j, as they do not have any physical meaning in some cases like: (i) extracting an average slope (C5) on time-resolved validation figures; (ii) extracting C1 and C2 criteria on normalized fuel decay profile, for which $x_{\text{fuel, normalized}} = 1$ at $t = 0$ s; (iii) extracting C1, C2, or C3 on temperature-resolved validation figures. Examples illustrating the extraction procedure with the obtained experimental and numerical criteria for both a time- and a temperature-resolved validation figure are presented in supplementary materials.

Table 3: Presentation of the five validation criteria with their respective usage.

Criteria	**Description**	**Used in**
C1	Time to peak maximum	Time-resolved data
C2	Time to peak half-maximum (before the peak)	Time-resolved data
C3	Time to peak half-maximum (after the peak)	Time-resolved data
C4	Area integration	Time- & temperature-resolved data
C5	Parameter=f(T), i.e., T slope	Temperature-resolved data

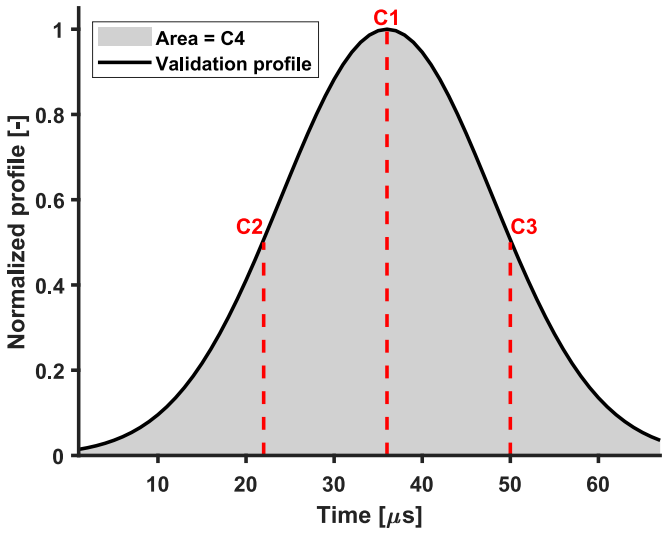

a) Time-resolved validation figure

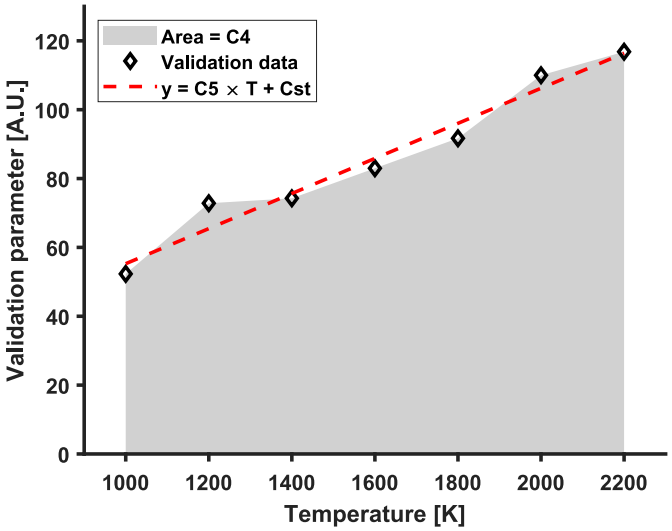

b) Temperature-resolved validation figure

Fig. 1. Examples presenting the extraction of the criteria from both time- (a) and temperature-resolved (b) validation figures. More detailed examples are provided in supplementary materials.

2.3.2. Calculation of the reaction model performance

The performances of the models were calculated by applying the objective function from Olm et al. [44] on the five validation criteria for each validation figure, as presented in Equation 1. As presented in [44], this error calculation method enables to quantify the experimental-simulation discrepancies with respect to the experimental uncertainty. In addition to the performance information, this methodology can also be employed to identify the submodels and the experimental conditions that require more effort for later model developments.

$$E_{\mathrm{C}i,j} = \left(\frac{\mathrm{C}i_{j,mod} - \mathrm{C}i_{j,exp}}{\delta(\mathrm{C}i_{j,exp})} \right)^2 \tag{1}$$

where $E_{\mathrm{C}i}$ is the objective function value for a specific criterion Ci for the validation figure j; $\delta(Ci_{j,exp})$ is the experimental uncertainty of the calculated criteria Ci for the given validation figure j, considering the acquisition system frequency, the detection technique used, and the non-ideality of the detection technique (finite laser beam dimensions and the collection angle of the optics). From all these sources of uncertainties, a global uncertainty is estimated based on the values reported in the literature (see details later in this section) and our own experience in conducting shock-tube experiments. Equation 1 was employed on C4 and C5, while Equation 2 was employed for C1, C2, and C3. As C1–C3 can be assimilated to delays, the use of this second equation is in line with the work of Olm et al.[44].

$$E_{\mathrm{C}i,j} = \left(\frac{\ln\left(\mathrm{C}i_{j,mod}\right) - \ln\left(\mathrm{C}i_{j,exp}\right)}{\ln\left(1 + \delta(\mathrm{C}i_{j,exp})/\mathrm{C}i_{j,exp}\right)} \right)^2 \tag{2}$$

For each criteria (i) and validation figure (j), the experimental uncertainty ($\delta(\mathrm{C}i_{j,exp})$) was determined. For C1–C3 criteria, the uncertainty was calculated based on their characteristic time scales. For short Ci delay ($\leq$ 50 μs), a 10 μs uncertainty was considered, while for long Ci delay ($>$ 50 μs), a 20% experimental uncertainty was used [64, 65, 66, 67]. δ_{C4} and δ_{C5} are more complicated to determine, as the uncertainties on both x- and y-axis (δ_x and δ_y, respectively) must be considered. For δ_x on time-resolved data, the same temporal uncertainty as the ones presented for C1–C3 criteria was considered, while a 1%-temperature-uncertainty was considered [68] for temperature-resolved data. As y-axis is exclusively related to species concentration, two δ_y-uncertainties are considered depending on the techniques used. For H profiles obtained with the ARAS technique, a 30% uncertainty is considered, while a 15% uncertainty is considered for SiH_2, SiH, Si, and SiH_4 profiles obtained with the

other techniques.

Table 4 and Fig. 2 summarize the different uncertainties calculations for the different criteria considered. The employed uncertainties (δ_x and δ_y) are provided in supplementary materials for each simulated condition. Note that changing the uncertainty values may slightly modify the final square root of the averaged objective functions (i.e., the SROF, described later in this section), whereas the final ranking of the models will remain the same. In Figs. 2a and 2b, δ_{C4} can be calculated by using the area difference between upper and lower envelope of the experimental signal, while δ_{C5} is obtained by mixing both the upper and lower boundaries. Detailed examples are provided in the supplementary materials to explain the calculation steps of the objective function for the different criteria.

Table 4: Summary of the experimental uncertainty calculation for each criteria and for the two types of data present in the validation dataset.

Criteria	**Time-resolved data**	**Temperature-resolved data**
C1–C3	Short time (≤ 50 μs): $\delta(\mathrm{C}i) = 10$ μs	-
	Long time (> 50 μs): $\delta(\mathrm{C}i) = 0.2 \times \mathrm{C}i$	-
C4	$\delta(\mathrm{C4}) = (\mathrm{C4_{upper}} - \mathrm{C4_{lower}})/2$	$\delta(\mathrm{C4}) = (\mathrm{C4_{upper}} - \mathrm{C4_{lower}})/2$
C5	-	$\delta(\mathrm{C5}) = (\mathrm{C5_{max}} - \mathrm{C5_{min}})/2$

Then, the global error was calculated by using the SROF, obtained from the square root of the averaged objective functions determined for each criterion and each validation figure j, as presented in Equation 3. This equation enables to perform both global (i.e., considering all the validation figures) and detailed analyses (i.e., per validation dataset or per measured species profiles) of the results by filtering the validation figures j.

$$SROF = \sqrt{\frac{1}{N_1 + N_2 + N_3 + N_4 + N_5} \times \left(\sum_{j=1}^{N_1} E_{\mathrm{C1},j} + \sum_{j=1}^{N_2} E_{\mathrm{C2},j} + \sum_{j=1}^{N_3} E_{\mathrm{C3},j} + \sum_{j=1}^{N_4} E_{\mathrm{C4},j} + \sum_{j=1}^{N_5} E_{\mathrm{C5},j} \right)} \quad (3)$$

where N_1, N_2, N_3, N_4, and N_5 correspond to the total number of validation figures for which C1, C2, C3, C4, and C5 are calculated. For some reaction models, criteria could not be extracted from the simulations and the objective function was not calculated for such conditions. Such conditions are met when a reaction model (i) cannot produce the measured chemical species, due to missing species or reaction pathways in the model, and (ii) when the conditions are outside the applicability range of the reaction model (such as the upper temperature limit of the Chebyshev reactions in Slakman model), and (iii) when the experimental and numerical profiles are too different (e.g., a peak shape experimentally *vs* a plateau shape numerically: C3 cannot be calculated numerically, so the corre-

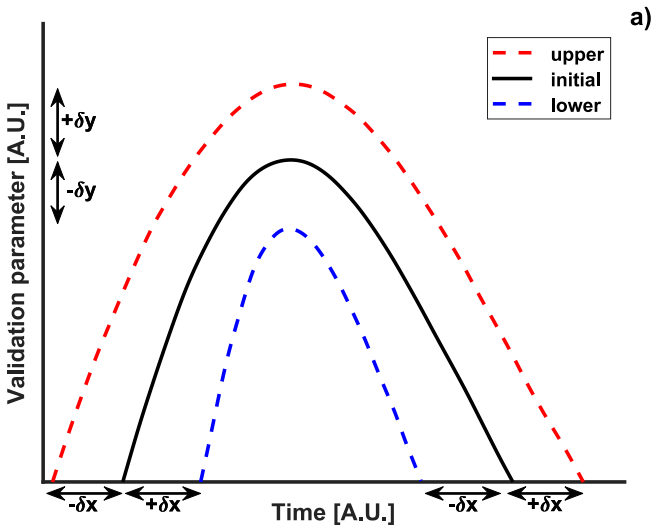

a) δ_{C4} calculation on time-resolved data

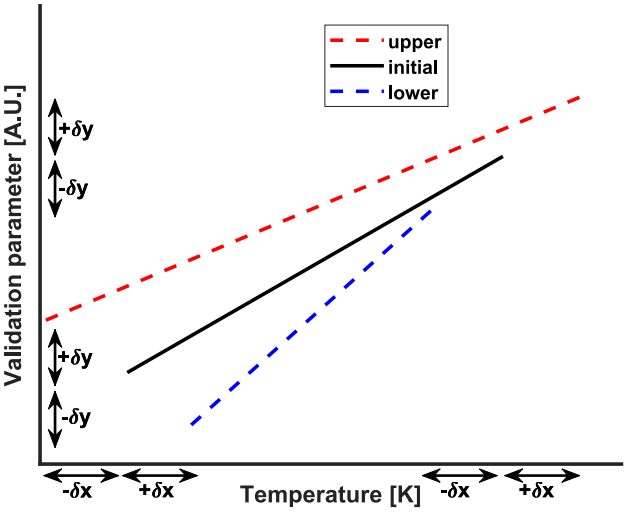

b) δ_{C4} calculation on temperature-resolved data

Fig. 2. Simplified representation of the initial experimental data with its uncertainty (upper and lower envelope) for both time- (a) and temperature-resolved data (b).

sponding objective function is considered as "NaN".) In fact, assigning an arbitrary value to these non-calculated criteria would have either highly promote (e.g., by assigning them as 0) or highly deprecate (e.g., by assigning them as a near-infinite value) the corresponding objective function results. Thus, SROF employs only validation figures j for which the criteria where calculated, while a "NaN" value is assigned for the objective functions of conditions with no calculated criteria. To have a meaningful comparison of the models, the models must have a similar fraction of "NaN", which must be as low as possible, as the fraction of "NaN" refers to the number of criteria (i.e., by extension the objective functions) that could not be extracted for a given model. As these fraction of non-estimated

criteria are not considered in the SROF calculation, the performance of a model with a low SROF and a high fraction of "NaN" can be misleading and the analysis of the results must be performed with the error distribution plot.

This error calculation method is preferred compared to the relative error calculation for the following reasons: (i) it accounts for the agreement of the models with respect to the experimental uncertainties; (ii) this calculation method promotes less the underestimating models than the relative error calculation, as pointed out previously [31]; (iii) the use of the SROF, instead of the objective function results, gives a direct access of how large is the error compared to the experimental uncertainty. Moreover, the error calculation method from Olm et al. [44] is dimensionless.

3. Results and Discussion

3.1. Qualitative agreement: examples of validations figures

Figure 3 presents the results obtained with the different reaction models for six typical validation figures for both silane and disilane pyrolysis with different species profiles. Some noteworthy points from these validation figures are: (i) overall, Chatelain's and Mével's reaction models are better reproducing the experimental data; (ii) except in some conditions, as presented in Fig. 3b, the corrected reaction model (Chatelain) better reproduces the experimental profiles than Mével's model; (iii) The RMG-based reaction model of Slakman captures well the silane and disilane pyrolysis experimental profiles, except for specific conditions for which the validation profiles are highly underestimated, see Fig. 3c. Due to the upper limit of the Chebyshev polynomial coefficients, some conditions could not be simulated with Slakman's reaction models, as seen in Fig. 3d and 3e. (iv) the other reference reaction models highly underestimate the experimental profiles in a large number of conditions, see Figs. 3a to 3d, with even opposite trends as compared to the experimental profiles in some cases, see Figs. 3e and 3f; (v) Kondo reaction model does not include disilane chemistry and its results are not represented in Figs. 3d and 3f for this reason. While SiH and Si species participate in several reactions in Kondo's reaction model, all these reactions are for oxidative conditions only, which explain the value equals to 0 in Fig. 3e.

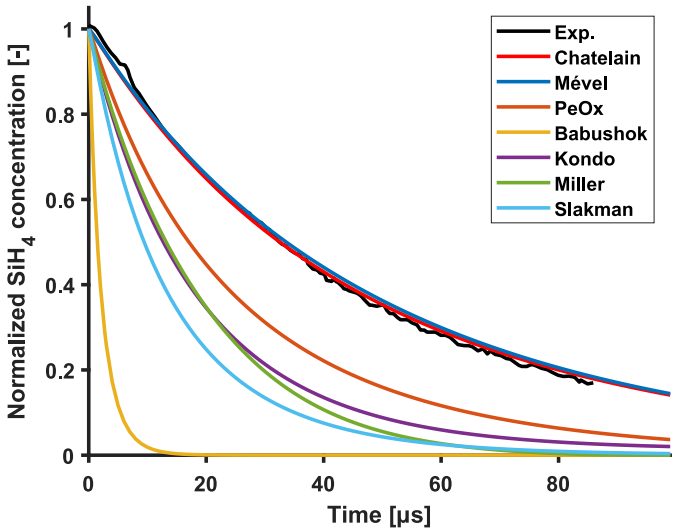

a) ST data from [23]: $X_{SiH_4} = 1000$ ppm, $X_{Ar} = 99.90\%$, $T = 1438$ K, and $P = 192.5$ kPa.

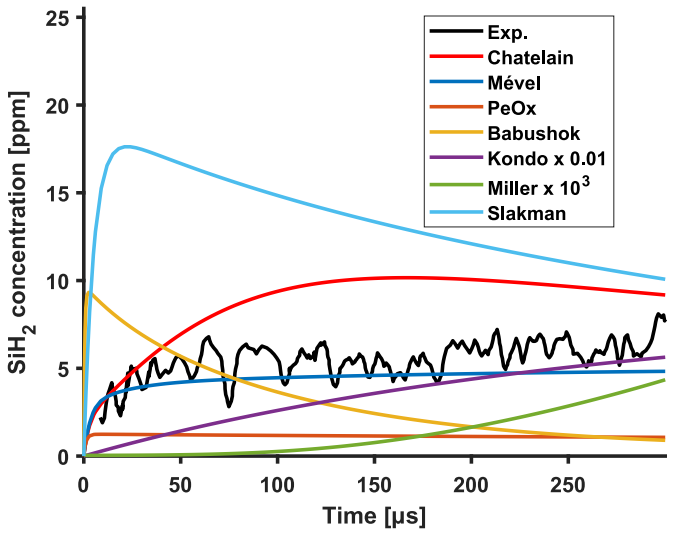

b) ST data from [23]: $X_{SiH_4} = 1000$ ppm, $X_{Ar} = 99.90\%$, $T = 1240$ K, and $P = 113.5$ kPa.

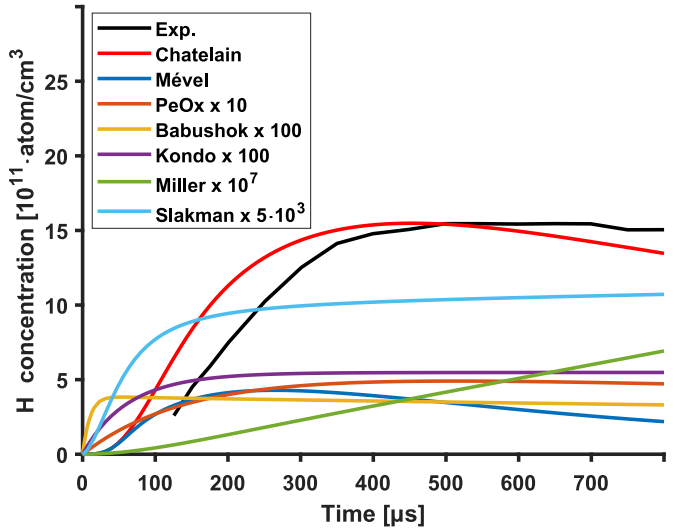

c) ST data from [46]: $X_{SiH_4} = 5$ ppm, $X_{Ar} > 99.99\%$, $T = 1336$ K, and $P = 146.9$ kPa.

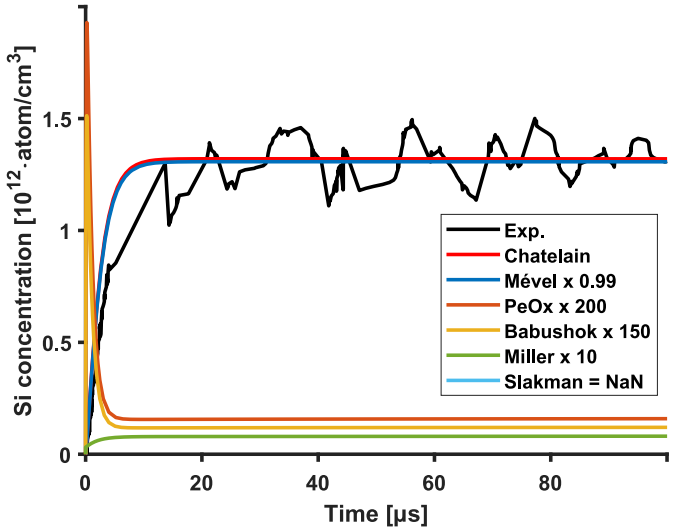

d) ST data from [53]: $X_{Si_2H_6} = 0.2$ ppm, $X_{Ar} > 99.99\%$, $T = 2185$ K, and $P = 100.0$ kPa.

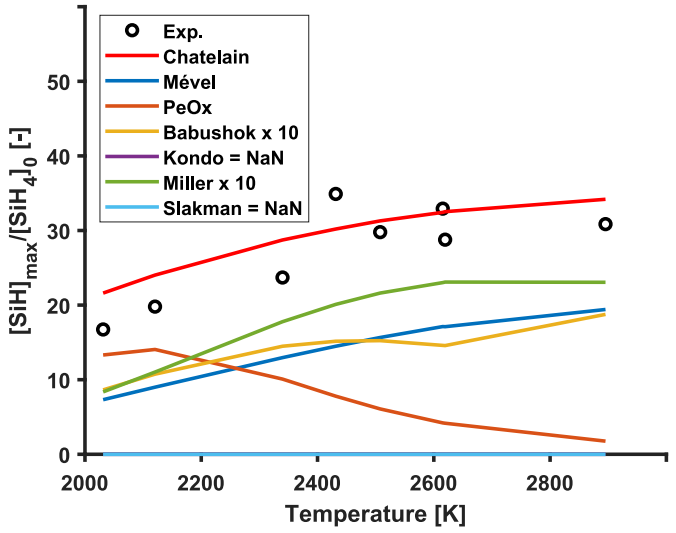

e) ST data from [21]: $X_{SiH_4} = 5$ ppm, $X_{H_2} = 500$ ppm, $X_{Ar} = 99.95\%$, $T = 2031$-2895 K, and $P = 93.0$-182.9 kPa.

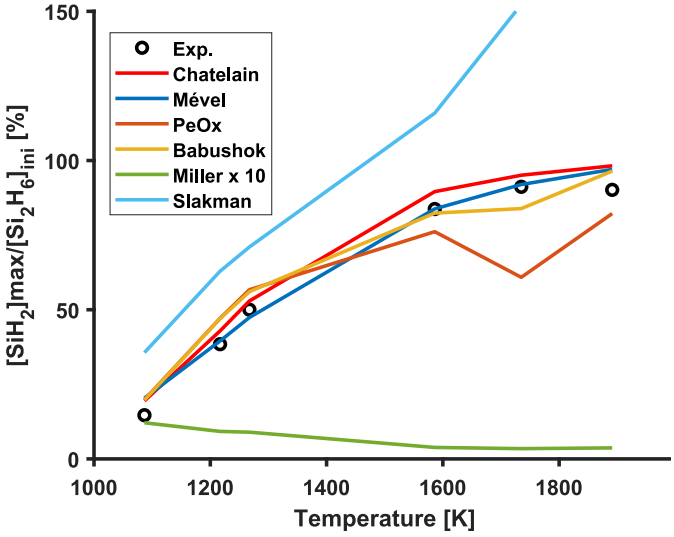

f) ST data from [49]: $X_{Si_2H_6} = 30$ ppm, $X_{Ar} > 99.99\%$, $T = 1087$-1891 K, and $P = 30.4$ kPa.

Fig. 3. Selected validation figures representative of both silane and disilane pyrolysis. ST stands for shock tube. Detailed information for each validation figures are available in supplementary materials.

3.2. *Quantitative analyses: global performances*

As explained in section 2.3.2, the global performances of the mechanisms evaluated by calculating the SROF from all the validation criteria extracted from all the validation figures. Table 5 and Fig. 4a summarizes both the results of the SROF for each criterion and also the global error to identify the mechanism with the lowest error. As the global error is an average value, Fig. 4b presents the distribution of the objective functions employed in the SROF calculation. Note that the objective function distribution is displayed in terms of the square root of the objective function values ($\sqrt{E_{Ci,j}}$) instead of the objective function values ($E_{Ci,j}$) to facilitate the discussion of the results. The "NaN" fraction reported in Fig. 4b refers to the fraction of conditions for which an objective function could not be calculated. In line with Olm's results, the model presenting the best agreement has on average a global error of 3 (an objective function of 10 is reported in Olm's work [44] for H_2-O_2 combustion with different diluents), which corresponds to an average error between the model predictions and the experimental data around three times the experimental uncertainty. This value is low compared to the reaction models with a fair performance that have a SROF of 10. In addition to this satisfactory global error, the reaction models with the lowest error (namely Chatelain, Mével, and Slakman) have a narrow error distribution in their objective functions. In fact, errors lower than 1 were obtained for more than 50% of the simulated criteria for Chatelain and Mével, 30% for Slakman, and below 20% for the other reaction models. For Chatelain and Mével models, this 50% value means that the error between the model and the experimental data is on average within the experimental uncertainty for nearly 50% of the cases. Except for Kondo's model which has a high SROF on C4 and no value on C5, the other reference reaction models do not estimate the peak position well (C1, C2, C3) except Miller's model for C2, while C4 and C5 seem better reproduced. In addition to the apparent low performance of Kondo's model, Kondo's results are significantly different from the other reaction models as: (i) they are obtained on the silane subset of data only, due to the absence of disilane chemistry in this reaction model; (ii) all temperature-resolved validation data involve species that are only formed in oxidative conditions in Kondo's reaction model, for which C5 criteria are not calculated. For this reason, C5 values are not reported in Table 5 and Fig. 4a; (iii) even with a reduced validation set (silane pyrolysis), the objective function cannot be calculated for more than 50% of the cases, due to its incomplete pyrolytic submodel.

Among all the reaction models tested, Chatelain's reaction model has the lowest global error value and has 74 % of its SROF values below two. This value is reduced to 72% and 71% for Mével and

Table 5: Comparison of the performances of the different reaction models. C1–C5 values represent the SROF calculated for each criterion and for each reaction model. The global error (Global) is obtained from Equation 3, considering all possible validation figures N_1, N_2, N_3, N_4, and N_5. The C1 error is obtained from Equation 3 by considering N_1 validation figures only. C2, C3, C4, and C5 are obtained similarly.

	Chatelain	**Mével**	**PeOx**	**Babushok**	**Kondo**	**Miller**	**Slakman**
C1	2	2.7	15.6	16.9	11.4	8.7	3.5
C2	4.2	5.9	11.6	17.8	17.8	4.3	7.4
C3	3.3	3.4	9.6	11.3	3.2	16.6	3.1
C4	2.6	2.3	4.4	2	167.3	2.9	2.2
C5	3.8	2	3.2	2.2	-	2.9	3.3
Global	3.1	3.4	9.8	11.7	110.6	8.3	4.1

Slakman reaction models, respectively. Chatelain, Mével, and Slakman reaction models have on average a global error 2-3 times lower than the other reaction model tested. In addition, the present results demonstrate the benefit in terms of prediction capability of the corrections applied to Mével's reaction model and the relevance of the correction methodology using collision limit violation analyses [34]. These results also evidence the weak performance of most of the reference reaction models for silane chemistry, which were not validated specifically on pyrolytic conditions. These weak performances of the reference reaction models may affect the current understanding on silane kinetics, due to the inaccurate model predictions for specific conditions.

3.3. Quantitative analyses: detailed analyses of the performances

Similar to the analyses performed in the previous section, the error (i.e., SROF) of the different reaction models were compared for different sets of data to identify the origin of their strengths and weaknesses. Table 6 compares the SROF values obtained for different subsets of data with the global SROF value (see previous section). In a first comparison, only the data corresponding to the two subsets of experimental data (corresponding to silane and disilane pyrolysis) were considered. In a second comparison, only the data considering a single type of species profiles were considered.

The results per subsets of data indicates that: (i) all reaction models have a lower global error on the disilane subset of data compared to the silane one; (ii) the reaction model ranking is identical on both subsets of data and is in agreement with the global error, which confirm the consistency of the global error and the absence of any averaging effect in the global ranking. The lower error of all models on disilane subset of data tends to indicate that either: disilane kinetics is better understood than silane kinetics or the experimental data present in the disilane subset of data have a larger relative uncertainty than in the silane subset. From our analyses, this apparent better performance seems induced by the higher relative experimental uncertainty in disilane subset of data, due to the higher

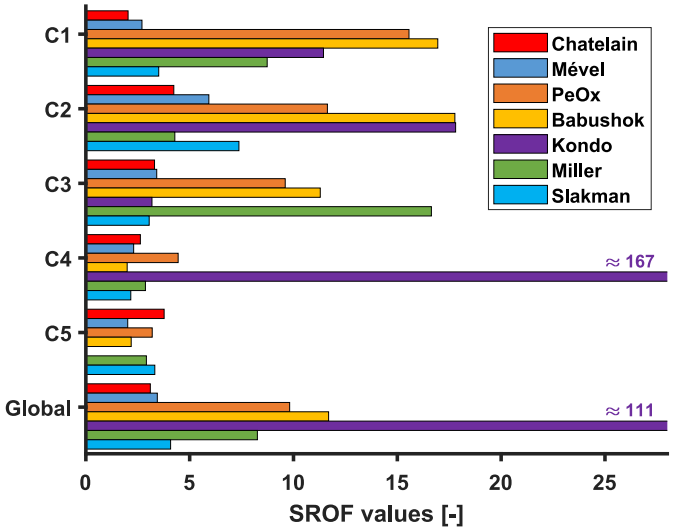

a) Global and criterion-specific SROF values

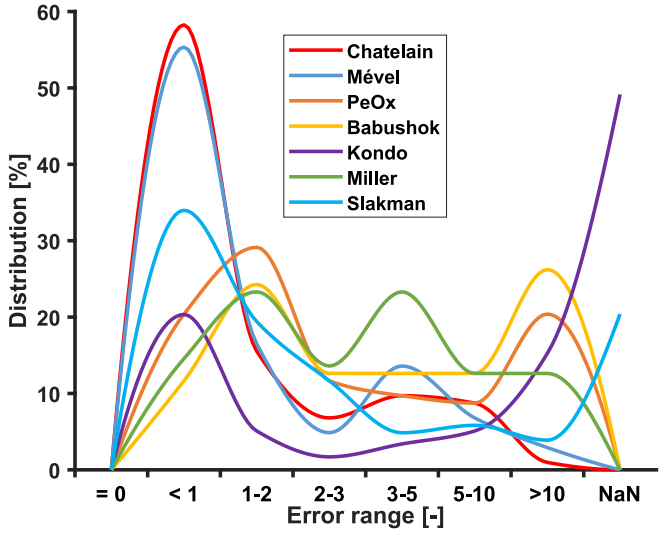

b) Distribution of the square root of the objective function ($\sqrt{E_{Ci,j}}$)

Fig. 4. Comparison of the overall performances of the different reaction models. In a), the different SROF values for each criteria are presented, as well as the global error. In b), the distribution of the of the values of the objective functions (i.e., employed in the SROF calculation) are presented. Note that the objective function distribution is displayed in terms of the square root of the objective function values ($\sqrt{E_{Ci,j}}$) instead of the objective function values ($E_{Ci,j}$) to facilitate the discussion of the results. Kondo's reaction model values are calculated on silane dataset only. "NaN" values refers to conditions for which an objective function cannot be calculated.

Table 6: Comparison of the performances of the reaction models for different subset of data, with respect to the global error defined for the overall data. The number of objective functions (# OF) refers to the number of individual objective function used to calculate the global error for each mechanism, except for Kondo and Slakman for which the number of objective functions are specified in brackets "()" with a and b superscripts, respectively.

	# OF	**Chatelain**	**Mével**	**PeOx**	**Babushok**	**Kondo**	**Miller**	**Slakman**
Global	103(30[a],82[b])	3.1	3.4	9.8	11.7	110.6	8.3	4.1
With silane or disilane conditions								
SiH_4	59(30[a],41[b])	3.9	4.4	11	13.8	110.6	8.6	5.5
Si_2H_6	44(0[a],41[b])	1.6	1.5	7.9	8	-	7.8	1.6
Per species profiles								
SIH_4	8(8[a,b])	1.4	1	1.1	8.4	2.3	1.9	3.1
SIH_2	54(10[a],54[b])	2.5	3	6.1	7.6	191	8.7	3.5
SIH	18(0[a],2[b])	3	3	12.9	10.5	-	12.4	5.5
SI	11(0[a],6[b])	1.2	1.3	15.1	19	-	2.4	1.9
H	12(12[a,b])	6.2	6.7	14.2	19.2	14.3	1.7	6.6

reactivity of disilane.

The results per species profiles point out the following aspects: (i) similar trends are observed with Chatelain's, Mével's, and Slakman's models which demonstrate the lowest global errors. However, a low error of Miller's model for H species profile dataset is observed, which is due to the overall good prediction of the peak positions in the H species profiles dataset. While the peak position is reproduced well overall, the quantity produced is several orders of magnitudes underestimated for all H profiles. This apparent good performance of Miller's model for this subset of data tends to indicate that the performance of each criterion might need to be weighted to obtain more representative global error values. The identification of the appropriated weights between each criterion is out of the scope of the present study. This also indicates that Olm's method is more appropriated to differentiate models with good to moderate performances, as $E_{Ci,j}$ has an asymptotic value for highly underestimated criteria ($\sim -Ci_{j,exp}/\delta(Ci_{j,exp})$); (ii) Except for the case of H atom species profiles (see previous discussion), the analyses per species profiles datasets confirm the previous global results and the overall good performance of Chatelain's, Mével's, and Slakman's reaction models. These analyses also confirm that the lower performances of the other reference reaction models is not due to a single dataset (i.e., SiH_4 or Si_2H_6 pyrolysis) or a specific set of species profiles.

3.4. Mechanism analyses

RoP analyses were conducted for Chatelain's, Mével's, Slakman's and PeOx's reaction models for two specific experimental conditions, which aim to be representative of silane and disilane pyrolysis.

While Miller has a better global error than PeOx, Miller's model is not selected for the flux diagram analyses due to its large discrepancy on Si atom production (underestimated by up to a factor of 10^6). The four selected reaction models are the top three mechanisms with the lowest global error and PeOx reaction model was considered as representative of all the other reaction models. In fact, the similarities between PeOx and Babushok reaction models were presented in our preliminary study [31, 32]. Only reactions contributing to more than 5% of the total species RoP are displayed, and their relative contribution is integrated over the experimental reaction time, which allows to obtain a single RoP value, independent of the reaction time for each validation condition analyzed. To keep the flux diagrams easily readable, only the main reaction pathways present in Chatelain's model (i.e., the model with the lowest global error) were considered. More complete versions of these two flux diagrams are available in the supplementary materials.

Figure 5 presents the main production and consumption pathways of SiH_4, SiH_2, SiH, Si, H during silane pyrolysis. Figure 5 highlights the following: (i) except two reactions ($SiH + SiH_4 = SiH_3 + SiH_2$ and $SiH + H = Si + H_2$), the flux diagrams between Chatelain and Mével's reaction models are nearly identical with only small differences in the value of each reaction relative contribution As both reactions were corrected in [34], the reaction pathways identified by Chatelain's has both more physical consistency and the lowest global error; (ii) while PeOx and the other less accurate reaction models have a higher global error, the first silane decomposition steps (including SiH_4 and SiH_2 decomposition steps and H_2, SiH_2, Si formation steps) are similar to Chatelain and Mével's reaction models. In fact, the discrepancies between the most accurate reaction model and the less accurate ones seem mostly due to the reaction $Si + SiH_2 = Si_2H + H$ and the reactions linking H, SiH, and SiH_3 species. Slakman reaction model has significantly different reaction pathways and only has in common the silane decomposition step with the other reaction models. These discrepancies with Chatelain's model are discussed later in this section.

Figure 6 presents the main production and consumption pathways of Si_2H_6, SiH_4, SiH_2, SiH, Si, and H obtained during disilane pyrolysis. Similar decomposition pathways are observed between both silane and disilane pyrolysis. Disilane decomposition step ($Si_2H_6 = SiH_4 + SiH_2$) adds to the main decomposition pathways of silane presented in Fig. 5. These similarities between the two decomposition pathways emphasizes the relevance of using both silane and disilane pyrolysis in the same validation dataset. Similar to the previous observations made for silane pyrolysis: (a) Chatelain and Mével's reaction model have similar reaction pathways with nearly identical relative contribution for each re-

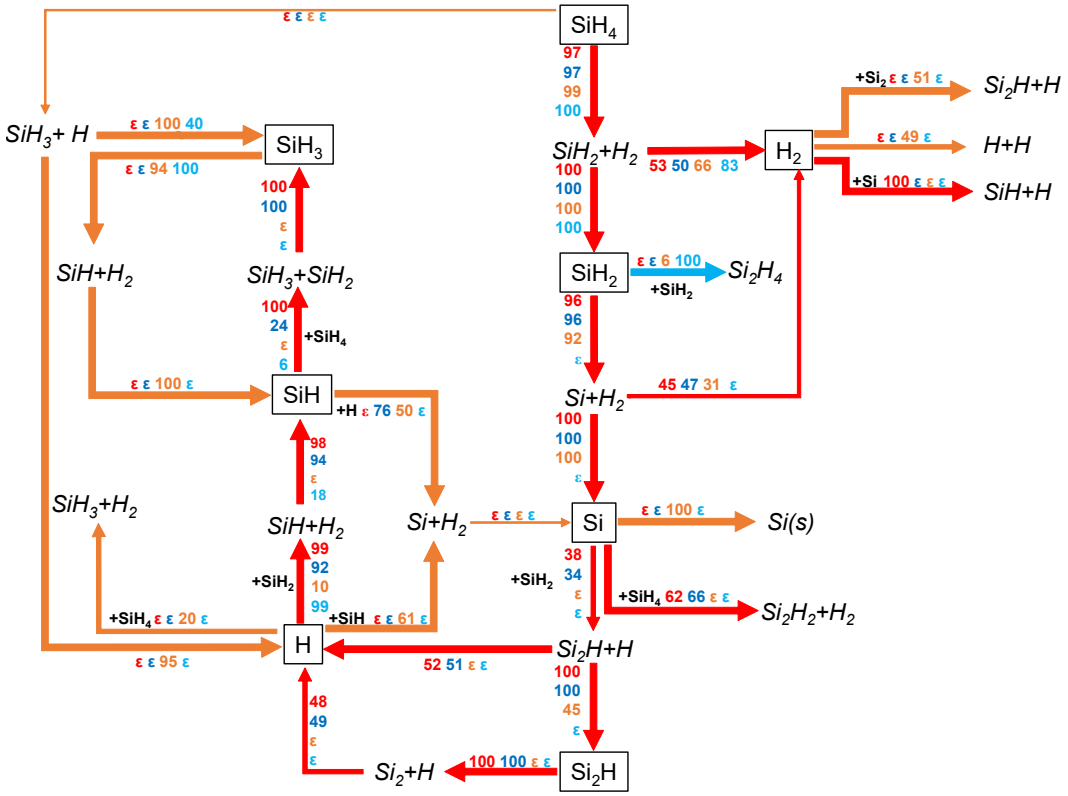

Fig. 5. Simplified flux diagram presenting the main reaction pathways during SiH_4 pyrolysis based on Chatelain's reaction model. The relative contribution of each reactions for each mechanism are presented in different colors: Chatelain in red, Mével in dark blue, PeOx in orange, and Slakman in light blue. ϵ stands for reactions that have a relative contribution under the 5% threshold. Conditions are $X_{SiH_4} = 0.2$ ppm, $X_{Ar} = 99.99998$ %, $T = 1405$ K, and $P = 64.8$ kPa.

actions; (b) PeOx show the same agreement with Chatelain and Mével's reaction pathways for SiH_4 and SiH_2 production and consumption pathways, as well as similar discrepancies in the consumption and production pathways for Si, H, SiH, and SiH_3. (c) as observed for silane, the four models share the same pathways only for the disilane and silane decomposition steps. Slakman reaction model again presents a specific decomposition pathway for disilane that is not observed in any of the other reaction models.

The previous observations made from RoP analyses are also confirmed by the sensitivity analyses results, i.e. the apparent similarity and discrepancies between the four models are confirmed. Figure 7 presents the normalized sensitivity analysis results for SiH_2 obtained with the four reaction models for silane and disilane pyrolysis, respectively in Figs. 7a and 7b. It is noted that: (i) the specificity of the reaction pathways in Slakman's model is confirmed with several highly sensitive reactions only present in Slakman's model. These reactions mainly involve Si_2H_4 isomers; (ii) The apparent similarities, identified from the RoP results, between Chatelain and Mével with PeOx models are

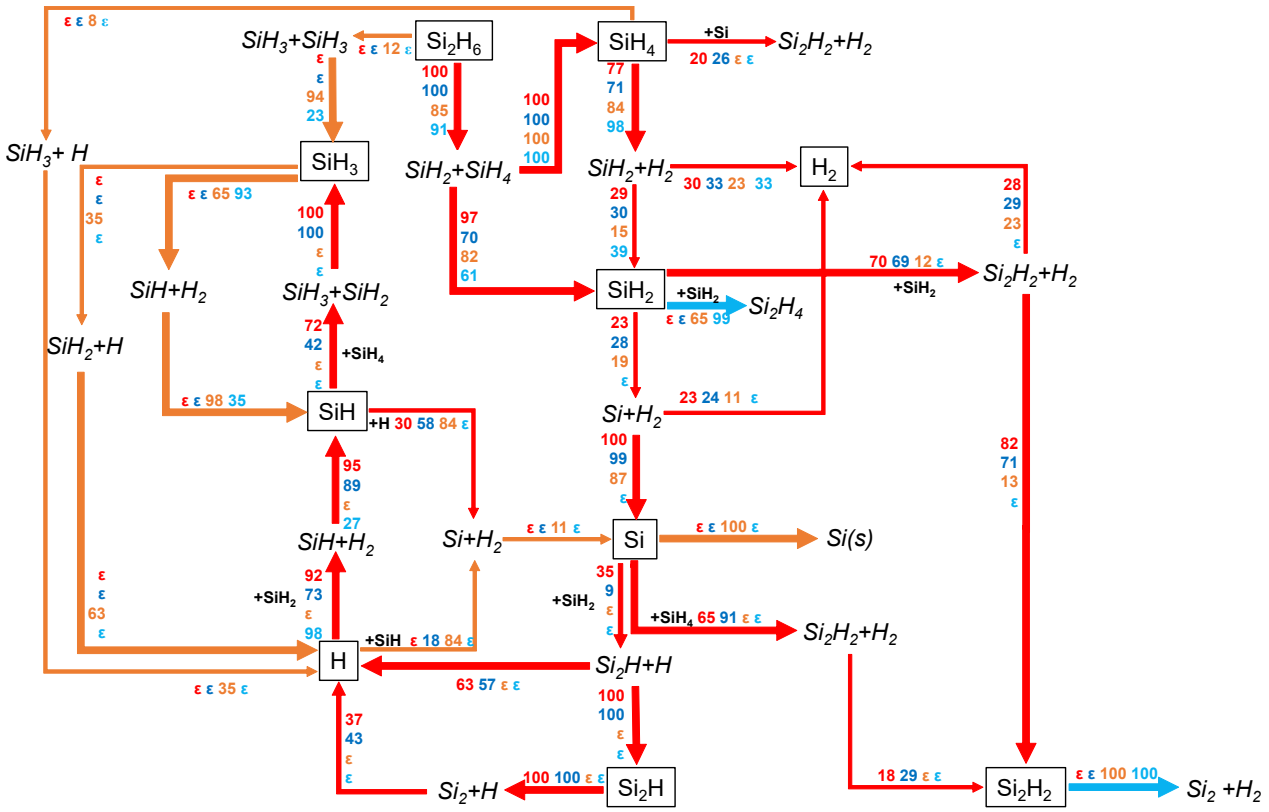

Fig. 6. Simplified flux diagram presenting the main reaction pathways during Si_2H_6 pyrolysis based on Chatelain's reaction model. The relative contribution of each reactions for each mechanism are presented in different colors: Chatelain in red, Mével in dark blue, PeOx in orange, and Slakman in light blue. ϵ stands for reactions that have a relative contribution under the 5% threshold. Conditions are: $X_{Si_2H_6} = 30$ ppm, $X_{Ar} = 99.997$ %, $T = 1580$ K, and $P = 29.6$ kPa.

confirmed with the similar most sensitive reactions for SiH_2 profiles in both conditions.

More critical analyses are provided in this section and aims to identify the origin of the differences between the models. First, an extensive comparison of the thermochemical data employed in the present models have been carried out in [34]. This comparison revealed that, on average, the 30 updated thermochemical data employed in Chatelain's model have a lower mean absolute error compared to thermochemical data employed in all the other reaction models. In addition, 13 unphysical reaction rates above the collision limit were corrected as well as 2 species mislabelling and 2 thermodynamic discontinuities. As discussed in [34], part of these inconsistencies are present in the other reaction models employed here. Thus, the updated thermodynamic data (calculated at a G4 theory level) and the refitted reaction rates employed in Chatelain's model should be preferred for later reaction model developments, as the thermochemical data have a higher accuracy and the rate constants are physically consistent (i.e., they are below the collision limit). Second, the solid particle formations are important aspects to consider for undiluted conditions, as presented in [69, 70]). Nevertheless, the

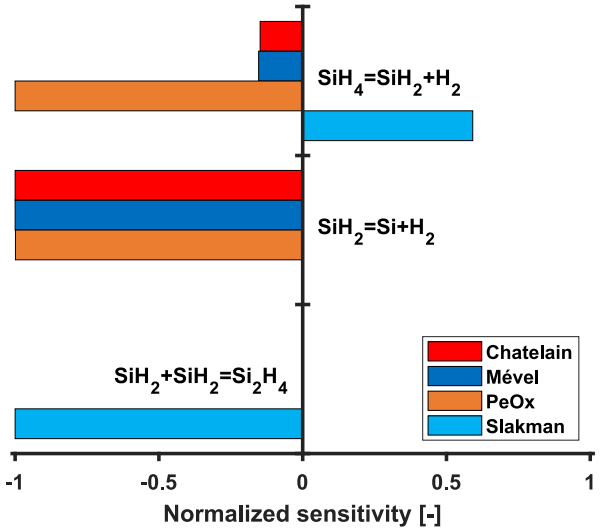

a) SiH_2 sensitivity analyses during silane pyrolysis

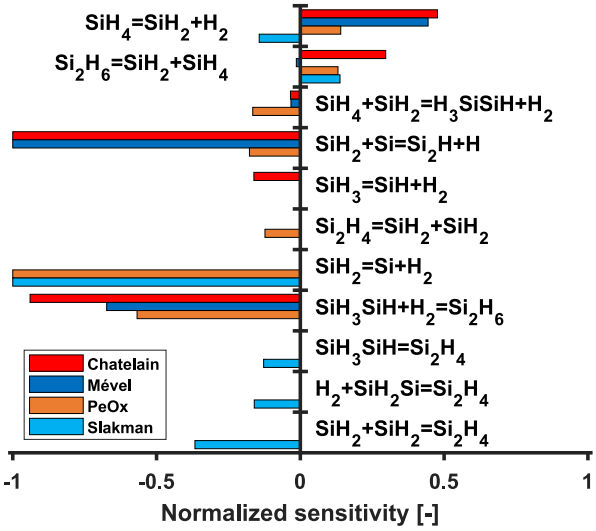

b) SiH_2 sensitivity analyses during disilane pyrolysis

Fig. 7. SiH_2 sensitivity analyses performed for silane (in a) and disilane (in b) with Chatelain, Mével, Slakman, and PeOx reaction models. Silane conditions (a) are: $X_{SiH_4} = 0.2$ ppm, $X_{Ar} = 99.99998$ %, $T = 1405$ K, and $P = 64.8$ kPa. Disilane conditions (b) are: $X_{Si_2H_6} = 30$ ppm, $X_{Ar} = 99.997$ %, $T = 1580$ K, and $P = 29.6$ kPa. Reactions displayed have an absolute normalized sensitivity coefficient above 0.1 in at least one reaction model.

lumped reaction presenting the direct solid Si formation from Si radical (Si=Si(s)) seems nonphysical both in term of chemical mechanism [71, 72] and in term of consumption rate. Indeed, Swihart and Girshick have shown theoretically that cyclic silicon hydrides structures are the most thermodynamically favorable precursors of solid silicon. Also, including the reaction Si=Si(s) taken from Babushok's model leads to a strong overprediction of the Si consumption rate (as observed in the validation figures 1-3 and 32 in the supplementary materials). For these reasons, this reaction is not present in both Chatelain's and Mével's model, while this reaction is historically present in silane's reaction models since Babushok's model. For later developments, a reaction mechanism describing the growth of solid silicon should be considered to enable the Si(s) formation at an appropriated production rate in both diluted and undiluted conditions, as included in Miller et al. [26] for silicon oxides or as performed for the soot formation in hydrocarbon combustion. The corresponding high error of PeOx's and Babushok's reaction models to reproduce Si and H species profiles (see Table 6) can be associated to this lumped reaction (i.e., the Si=Si(s) reaction). Third, the significantly different reaction pathways obtained with Slakman's model are mainly due to the reaction $SiH_2 + SiH_2 = Si_2H_4$ (with Si_2H_4 referring to $SiH_2-SiH_2(S)$), as evidenced in Figs. 5, 6, and 7. From the information available in the model, the reaction currently employed in Slakman's model is based on the work of Giunta et al. [30], while a more recent rate constant was proposed by Dollet et al. [73]. Updating this reaction with the value from Dollet et al. [73] reduced by 1 million fold both the forward and backward rate constants associated to this reaction within this range of conditions (P = 0.1 - 10bar and T = 500 - 4000 K). As a consequence, the pathway leading to $Si_2H_4(S)$ ($SiH_2 + SiH_2 = Si_2H_4$) in Fig. 5 becomes negligible with the updated rate constant. This finding is in agreement with Fig. 7, where this reaction was identified as very sensitive. Furthermore, a few noteworthy points indicate that Slakman's model (or the RMG database employed to generate the mechanism) needs additional improvements, as: (i) Slakman's model is the only reaction model to have a significantly lower formation enthalpy for both silane (23.3 kJ/mol, while 34.1, 34.1, and 31.4 kJ/mol are reported experimentally, numerically, and at G4 theory level [34], respectively) and disilane (66.8 kJ/mol, while 78.4, 79.2, and 74.9 kJ/mol are reported experimentally, numerically, and at G4 theory level [34], respectively). Even a 15-kJ/mol difference is observed on the formation enthalpy of Si_3H_6 between Slakman's model and the G4 calculations. All these values were collected from literature data and recently reported [34]. One possible explanation of such discrepancies is that the silane's, disilane's, and trisilane's formation enthalpy had to be underestimated to improve the validity range of the group additivity method employed in RMG

over a large set of Si-containing molecules. In addition, some state-specific species have a large discrepancy in their formation enthalpies which are not in agreement with the literature data and the G4 values reported in [34], such as Si_2 (Si_2(S) is at 461.5 and 631.8 kJ/mol for Slakman's model and the G4 calculation) and Si_2H_2 (H_2SiSi(S) is at 371.1 and 440.8 kJ/mol for Slakman's model and G4 calculation, respectively). While some others state specific formation enthalpies are in agreement with literature, these discrepancies may indicate either a problem in the group additivity increments employed in RMG to calculate the thermochemistry for different electronic states or a lack of data in the database. The state specific data reported in [34] could be employed to improve the thermochemistry estimation. Nevertheless, this first RMG-based reaction model shows promising results compared to most of the reference reaction models, while some aspects of the RMG database still need further refinements (as presented earlier in this section).

Based on error score and the analyses performed on the present validation dataset, the decomposition pathways proposed by Chatelain's model seems the most reliable one among all the tested models. New experimental data focused on less diluted conditions or employing other validation profiles (e.g., Si_2H_4 isomers: Si_2H_4(S), Si_2H_4(T), SiH_3-SiH(S),SiH_3-SiH(T) or Si_2H_2 isomers: Si_2H_2 and SiH_2Si) could confirm this trend. Such an achievement is extremely challenging given the limited knowledge on the spectroscopic properties of silicon hydrides as compared to hydrocarbon species. Thus, numerical studies focused on the identification of the reaction kinetics of all stable (cyclic or bridged) isomers or the state-specific species could be beneficial for later model developments, as they would most likely involve lower energy barriers kinetics. Both aspects are out of the scope of the present paper.

4. Conclusions

In the present study, we evaluated seven reaction models against a large validation dataset for silane (SiH_4) and disilane (Si_2H_6) pyrolysis (85 individual conditions). The novelties of this work are the use of the comprehensive validation dataset (7 reaction models and 85 conditions), the multiple validation criteria (considering the shape and the quantity of the validation profile), and the use of an error calculation method accounting for the experimental uncertainty (based on Olm et al. [44]) to assess the performance of the models on silane and disilane pyrolysis. The major findings can be summarized as follow:

- Overall, Chatelain's reaction model presents both the lowest global error (3.1) and the highest fraction (74%) of criteria predicted within two times the experimental uncertainty.
- Mével's model has the second lowest global error (3.4) and the second highest fraction (72%) of criteria predicted within two times the experimental uncertainty.
- Except Slakman's model, which also has a fair global error (4.1), all the other reaction models present large discrepancies with the validation dataset, with a global error above 8 (nearly 10 for most of them) and up to 110 for Kondo's model.
- The performances of the first RMG-based reaction model (Slakman) are encouraging, as this reaction model is the first RMG-based reaction model (Slakman's model) for Si_XH_y chemical system. However, some aspects of thermochemical data and the kinetic rate estimation seem to need revision.
- From our analyses, the decomposition pathways presented by Chatelain's and Mével's models are nearly identical and are the most reliable to represent the high-temperature kinetics of silane and disilane, based on the experimental data currently available in the literature.
- To further support the present results, new experimental data could be focused on obtaining similar results in less-diluted (e.g., near 70%-dilution) conditions or state-specific validation profiles (e.g, Si_2H_4(S) and Si_2H_4(T)).

As most of the reference reaction models have a high global error on silane pyrolysis, the current understanding of silane oxidation kinetics may be impacted by the inaccurate model prediction for specific conditions (high temperature and equivalence ratio conditions). The present conclusions will be compared to the results of the second part of the study on silane oxidation [45]. The present work focusing on shock tube experiments has been completed by flame speed measurements for hydrogen-nitrous oxides mixtures with and without silane addition, see [69, 70]. Under these conditions, Chatelain's model also performed well and the condensation process of solid silicon oxides has been shown to play a significant impact.

Acknowledgment

The research reported in this publication was supported by funding from King Abdullah University of Science and Technology (KAUST). Rémy Mével was supported by a start-up funding from the Cen-

ter for Combustion Energy from Tsinghua University and the 1000 Young Talent of China program. Yizhuo He was funded by China Postdoctoral Science Foundation (grant number 2019M650674). The authors are gratefull to Mustapha Fikri, Institut für Verbrennung und Gasdynamik, for providing Hans-Juergen Mick's PhD thesis manuscript.

Supplementary Materials

The supplementary materials include the following items:

- Step-by-step examples presenting the extraction of the criteria and the associated error calculations
- Comprehensive reaction pathway diagrams for silane and disilane pyrolysis
- A table summarizing the conditions of all the experimental conditions
- Plots of all the validation figures including all the experimental and calculated profiles
- The reaction models used in Chemkin format

References

[1] Y.-B. Park, S.-W. Rhee, Low temperature silicon dioxide film deposition by remote plasma enhanced chemical vapor deposition: growth mechanism, Surface and Coatings Technology 179 (2-3) (2004) 229–236.

[2] J. Westwater, D. P. Gosain, S. Tomiya, S. Usui, H. Ruda, Growth of silicon nanowires via gold/silane vapor-liquid-solid reaction, Journal of Vacuum Science and Technology B: Microelectronics and Nanometer Structures 15 (3) (1997) 554–557.

[3] M. Shao, D. D. D. Ma, S.-T. Lee, Silicon nanowires - synthesis, properties, and applications, European Journal of Inorganic Chemistry (27) (2010) 4264–4278.

[4] H. J. Curran, E. M. Fisher, P.-A. Glaude, N. M. Marinov, W. J. Pitz, C. K. Westbrook, D. W. Layton, P. F. Flynn, R. P. Durrett, A. O. Zur Loye, O. C. Akinyemi, F. L. Dryer, Detailed chemical kinetic modeling of diesel combustion with oxygenated fuels, SAE Transactions 110 (2001) 514–521.

[5] P. Dagaut, C. Togbé, Experimental and modeling study of the kinetics of oxidation of ethanol−gasoline surrogate mixtures (E85 surrogate) in a jet-stirred reactor, Energy & Fuels 22 (5) (2008) 3499–3505.

[6] W. K. Metcalfe, S. Dooley, F. L. Dryer, Comprehensive detailed chemical kinetic modeling study of toluene oxidation, Energy & Fuels 25 (11) (2011) 4915–4936.

[7] L. Sy Tran, B. Sirjean, P.-A. Glaude, R. Fournet, F. Battin-Leclerc, Progress in detailed kinetic modeling of the combustion of oxygenated components of biofuels, Energy 43 (1) (2012) 4–18.

[8] R. Mével, K. Chatelain, P. A. Boettcher, G. Dayma, J. E. Shepherd, Low temperature oxidation of n-hexane in a flow reactor, Fuel 126 (2014) 282–293.

[9] K. Chatelain, R. Mével, S. Menon, G. Blanquart, J. E. Shepherd, Ignition and chemical kinetics of acrolein–oxygen–argon mixtures behind reflected shock waves, Fuel 135 (2014) 498–508.

[10] C. W. Gao, A. G. Vandeputte, N. W. Yee, W. H. Green, R. E. Bonomi, G. R. Magoon, H.-W. Wong, O. O. Oluwole, D. K. Lewis, N. M. Vandewiele, K. M. van Geem, JP-10 combustion studied with shock tube experiments and modeled with automatic reaction mechanism generation, Combustion and Flame 162 (8) (2015) 3115–3129.

[11] R. Mével, K. Chatelain, G. Blanquart, J. E. Shepherd, An updated reaction model for the high-temperature pyrolysis and oxidation of acetaldehyde, Fuel 217 (2018) 226–239.

[12] K. Chatelain, M. Matrat, L. Catoire, M. Bouchez, Development of kinetic models for the hybrid fuels combustion containing aluminum particles, Journal of Propulsion and Power 35 (2) (2019) 443–450.

[13] C. Schulz, T. Dreier, M. Fikri, H. Wiggers, Gas-phase synthesis of functional nanomaterials: challenges to kinetics, diagnostics, and process development, Proceedings of the Combustion Institute (2018).

[14] L. G. Britton, Combustion hazards of silane and its chlorides, Plant/Operations Progress 9 (1) (1990) 16–38.

[15] E. Y. Ngai, K. P.-P. Huang, J.-R. Chen, C.-C. Shen, H.-Y. Tsai, S.-K. Chen, S.-C. Hu, P.-Y. Yeh, C.-D. Liu, Y.-Y. Chang, D.-J. Peng, H.-C. Wu, Field tests of release, ignition, and explosion from silane cylinder valve and gas cabinet, Process Safety Progress 26 (4) (2007) 265–282.

[16] V. L. Rausch, C. R. McClinton, J. L. Crawford, Hyper-X: flight validation of hypersonic air-breathing technology, in: ISABE 97, 1997, paper 7024.

[17] R. Zubrin, T. Muscatello, B. Birnbaum, K. Caviezel, G. Snyder, M. Berggren, Progress in mars ISRU technology, in: 40th AIAA Aerospace Sciences Meeting & Exhibit, 2002, p. 461, paper 2002-0461.

[18] A. G. McLain, C. J. Jachimowski, R. C. Rogers, Ignition of SiH_4-H_2-O_2-N_2 behind reflected shock waves, TP-2114 (1983).

[19] J. R. Hartman, J. Famil-Ghiriha, M. A. Ring, H. E. O'Neal, Stoichiometry and possible mechanism of SiH_4-O_2 explosions, Combustion and Flame 68 (1) (1987) 43–56.

[20] J. A. Britten, J. Tong, C. K. Westbrook, A numerical study of silane combustion, in: Symposium (International) on Combustion, Vol. 23, 1991, pp. 195–202.

[21] H.-J. Mick, Untersuchungen zur kinetic elementarer reaktionen in silanereaktionssystemen basierend auf atom- und molekulspektroskopischen messungen, Ph.D. thesis, University of Duisburg (1995).

[22] D. Woiki, L. Catoire, P. Roth, High-temperature kinetics of si-containing precursors for ceramic processing, AIChE Journal 43 (S11) (1997) 2670–2678.

[23] E. L. Petersen, M. W. Crofton, Measurements of high-temperature silane pyrolysis using SiH_4 IR emission and SiH_2 laser absorption, The Journal of Physical Chemistry A 107 (50) (2003) 10988–10995.

[24] V. I. Babushok, W. Tsang, D. R. Burgess, M. R. Zachariah, Numerical study of low- and high-temperature silane combustion, Proceedings of the Combustion Institute 27 (2) (1998) 2431–2439.

[25] S. Kondo, K. Tokuhashi, A. Takahashi, M. Kaise, A numerical study of low temperature silane combustion, Combustion Science and Technology 159 (1) (2000) 391–406.

[26] T. A. Miller, M. S. Wooldridge, J. W. Bozzelli, Computational modeling of the $SiH_3 + O_2$ reaction and silane combustion, Combustion and Flame 137 (1-2) (2004) 73–92.

[27] R. Mével, Étude de mécanismes cinétiques et des propriétés explosives des systèmes hydrogène-protoxyde d'azote et silane-protoxyde d'azote : application à la sécurité industrielle, Ph.D. thesis, Université d'Orléans (2009).

[28] S. Javoy, R. Mével, G. Dupré, Oxygen atom kinetics in silane–hydrogen–nitrous oxide mixtures behind reflected shock waves, Chemical Physics Letters 500 (4-6) (2010) 223–228.

[29] R. Mével, S. Javoy, G. Dupré, A chemical kinetic study of the oxidation of silane by nitrous oxide, nitric oxide and oxygen, Proceedings of the Combustion Institute 33 (1) (2011) 485–492.

[30] C. J. Giunta, J. D. Chapple-Sokol, R. G. Gordon, Kinetic modeling of the chemical vapor deposition of silicon dioxide from silane or disilane and nitrous oxide, Journal of The Electrochemical Society 137 (10) (1990) 3237–3253.

[31] K. P. Chatelain, R. Alharbi, R. Mével, E. L. Petersen, D. A. Lacoste, An accurate reaction model for the high-temperature pyrolysis of silane and disilane, in: 11th US National Combustion Meeting, Pasadena, USA, 2019.

[32] K. P. Chatelain, R. Alharbi, R. Mével, E. L. Petersen, D. A. Lacoste, Assessment of reference reaction models relevant for the oxidation of SiH_4 with O_2 against a comprehensive validation database, in: 12th Asia-Pacific Conference on Combustion, Fukuoka, Japan, 2019.

[33] B. L. Slakman, H. Simka, H. Reddy, R. H. West, Extending reaction mechanism generator to silicon hydride chemistry, Industrial & Engineering Chemistry Research 55 (49) (2016) 12507–12515.

[34] K. P. Chatelain, R. Mével, D. A. Lacoste, Correction of reaction models using collision limit violation analyses: Application to a silane reaction model, Combustion and Flame 217 (2020) 346 – 359.

[35] K. Chatelain, Oxidation stability of fuels in liquid phase, Ph.d. thesis, Université Paris-Saclay (2016).

[36] K. Chatelain, A. Nicolle, A. Ben Amara, L. Catoire, L. Starck, Wide range experimental and kinetic modeling study of chain length impact on n-alkanes autoxidation, Energy & Fuels 30 (2) (2016) 1294–1303.

[37] K. Chatelain, A. Nicolle, A. Ben Amara, L. Starck, L. Catoire, Structure–reactivity relationships in fuel stability experimental and kinetic modeling study of isoparaffin autoxidation, Energy & Fuels 32 (9) (2018) 9415–9426.

[38] S. Park, Y. Wang, S. H. Chung, S. M. Sarathy, Compositional effects on pah and soot formation in counterflow diffusion flames of gasoline surrogate fuels, Combustion and Flame 178 (2017) 46 – 60.

[39] W. Pejpichestakul, A. Frassoldati, A. Parente, T. Faravelli, Kinetic modeling of soot formation in premixed burner-stabilized stagnation ethylene flames at heavily sooting condition, Fuel 234 (2018) 199 – 206.

[40] T. Zhang, L. Zhao, M. R. Kholghy, S. Thion, M. J. Thomson, Detailed investigation of soot formation from jet fuel in a diffusion flame with comprehensive and hybrid chemical mechanisms, Proceedings of the Combustion Institute 37 (2) (2019) 2037 – 2045.

[41] B. Hidding, M. Pfitzner, Rocket propellant characteristics of silanes/O_2, Journal of Propulsion and Power 22 (4) (2006) 786–789.

[42] B. Hidding, M. Fikri, M. Bozkurt, C. Schulz, T. Soltner, A. Kornath, M. Pfitzner, M. Lang, A. J. Adamczyk, L. Broadbelt, H. Ellerbrock, D. Simone, C. Bruno, Spiking of hydrocarbon fuels with silanes-based combustion enhancers, Transactions of the Japan Society for Aeronautical and Space Sciences, Aerospace Technology Japan 8 (2010) 39–45.

[43] W. A. Eger, A. Genest, N. Rösch, Thermal decomposition of branched silanes: A computational study on mechanisms, Chemistry 18 (29) (2012) 9106–9116.

[44] C. Olm, I. G. Zsély, R. Pálvölgyi, T. Varga, T. Nagy, H. J. Curran, T. Turányi, Comparison of the performance of several recent hydrogen combustion mechanisms, Combustion and Flame 161 (9) (2014) 2219–2234.

[45] K. P. Chatelain, Y. He, S. Javoy, R. Mével, E. L. Petersen, D. A. Lacoste, Current status of the high-temperature kinetic models of silane: Part II. Oxidation, *Submitted to Combustion and Flame* (2020).

[46] H. J. Mick, V. N. Smirnov, P. Roth, Aras measurements on the thermal decomposition of silane, Berichte der Bunsengesellschaft für physikalische Chemie 97 (6) (1993) 793–798.

[47] H. J. Mick, P. Roth, V. N. Smirnov, I. S. Zaslonko, Formation of hydrogen atoms in silane pyrolysis behind shock waves, kinetics and thermochemistry of SiH_4, SiH_3, and SiH_2 decomposition, Kinetics and catalysis 35 (4) (1994) 439–451.

[48] M. W. Markus, P. Roth, A quantitative ring dye laser absorption diagnostic for free SiH_2 (X^1A_1) radicals at high temperatures, Journal of Quantitative Spectroscopy and Radiative Transfer 52 (6) (1994) 783–789.

[49] M. W. Markus, P. Roth, Development of a quantitative ring dye laser absorption diagnostic for free SiH radicals, Journal of Quantitative Spectroscopy and Radiative Transfer 56 (4) (1996) 489–499.

[50] E. Petersen, M. Crofton, Ignition and oxidation of dilute silane-oxidizer mixtures behind reflected shock waves, in: 38th AIAA/ASME/SAE/ASEE Joint Propulsion Conference & Exhibit, 2002, paper 3875.

[51] E. L. Petersen, D. M. Kalitan, M. J. A. Rickard, Reflected-shock ignition of $SiH_4/H_2/O_2/Ar$ and $SiH_4/CH_4/O_2/Ar$ mixtures, Journal of Propulsion and Power 20 (4) (2004) 665–674.

[52] M. W. Crofton, E. L. Petersen, Frequency modulation spectroscopy in a particle-forming environment for the detection of SiH_2, Proceedings of the Combustion Institute 30 (1) (2005) 1583–1589.

[53] H.-J. Mick, M. W. Markus, P. Roth, V. N. Smirnov, A shock tube study of the thermal decomposition of Si_2H_6 based on Si and SiH_2 measurements, Berichte der Bunsengesellschaft für physikalische Chemie 99 (6) (1995) 880–890.

[54] E. L. Petersen, D. M. Kalitan, M. J. A. Rickard, M. W. Crofton, Silane oxidation behind reflected shock waves, in: Z. Jiang (Ed.), Shock waves, Springer, Berlin, 2005, pp. 585–590.

[55] J. M. Hall, S. Reehal, E. L. Petersen, Kinetics of OH chemiluminescence in the presence of silicon, Chemical Physics Letters 425 (4-6) (2006) 229–233.

[56] C. W. Gao, J. W. Allen, W. H. Green, R. H. West, Reaction mechanism generator: automatic construction of chemical kinetic mechanisms, Computer Physics Communications 203 (2016) 212–225.

[57] ANSYS, Academic research mechanical, release 18.2.

[58] D. G. Goodwin, R. L. Speth, H. K. Moffat, B. W. Weber, Cantera: An object-oriented software toolkit for chemical kinetics, thermodynamics, and transport processes, www.cantera.org, version 2.4.0 (2018).

[59] W. Green, et al., RMG documentation release 3.1.
URL reactionmechanismgenerator.github.io/RMG-Py/index.html

[60] C. J. Jachimowski, A. G. McLain, A chemical kinetic mechanism for the ignition of silane/hydrogen mixtures, TP-2129 (1983).

[61] M. R. Zachariah, W. Tsang, Theoretical calculation of thermochemistry, energetics, and kinetics of high-temperature $Si_xH_yO_z$ reactions, The Journal of Physical Chemistry 99 (15) (1995) 5308–5318.

[62] M. D. Allendorf, C. F. Melius, P. Ho, M. R. Zachariah, Theoretical study of the thermochemistry of molecules in the Si-O-H system, The Journal of Physical Chemistry 99 (41) (1995) 15285–15293.

[63] Y. Hidaka, H. Takuma, M. Suga, Shock-tube study of the rate constant for excited hydroxyl $OH^{\star\,2}\Sigma^+$) formation in the N_2O-H_2 reaction, The Journal of Physical Chemistry 89 (23) (1985) 4903–4905.

[64] S. M. Sarathy, G. Kukkadapu, M. Mehl, W. Wang, T. Javed, S. Park, M. A. Oehlschlaeger, A. Farooq, W. J. Pitz, C.-J. Sung, Ignition of alkane-rich face gasoline fuels and their surrogate mixtures, Proceedings of the Combustion Institute 35 (1) (2015) 249–257.

[65] O. Mathieu, B. Giri, A. Agard, T. Adams, J. Mertens, E. Petersen, Nitromethane ignition behind reflected shock waves: Experimental and numerical study, Fuel 182 (2016) 597 – 612.

[66] D. Kalitan, J. Hall, E. Petersen, Ignition and oxidation of ethylene-oxygen-diluent mixtures with and without silane, Journal of Propulsion and Power 21 (6) (2005) 1045–1056.

[67] Y. Zhu, D. Davidson, R. Hanson, 1-butanol ignition delay times at low temperatures: An application of the constrained-reaction-volume strategy, Combustion and Flame 161 (3) (2014) 634–643.

[68] D. F. Davidson, Z. Hong, G. L. Pilla, A. Farooq, R. D. Cook, R. K. Hanson, Multi-species time-history measurements during n-dodecane oxidation behind reflected shock waves, Proceedings of the Combustion Institute 33 (1) (2011) 151–157.

[69] R. Mével, K. Chatelain, Y. He, S. Lapointe, D. Lacoste, M. Allix, N. Chaumeix, C. Paillard, Combustion of silane-nitrous oxide-argon mixtures: analysis of laminar flame propagation and condensed products, Proceedings of the Combustion Institute, *In press* (2020). doi:10.1016/j.proci.2020.06.381.

[70] R. Mével, K. Chatelain, S. Lapointe, D. Lacoste, M. Idir, D. G., N. Chaumeix, Spherically expanding flame in silane-hydrogen-nitrous oxide-argon mixtures, Combustion and Flame 221 (2020) 150–159.

[71] M. Swihart, S. Girshick, Thermochemistry and kinetics of silicon hydride cluster formation during thermal decomposition of silane, Journal of Physical Chemistry B 103 (1999) 64–76.

[72] M. Swihart, S. Girshick, Ab initio structures and energetics of selected hydrogenated silicon clusters containing six to ten silicon atoms, Chemical Physics Letters 307 (1999) 527–532.

[73] A. Dollet, S. de Persis, Pressure-dependent rate coefficients of chemical reactions involving Si_2H_4 isomerization from QRRK calculations, Journal of Analytical and Applied Pyrolysis 80 (2) (2007) 460–470.